Chapter 4 Tight Binding Approximation

Chapter 4 .1 Background

Calculation of tunneling currents in some materials systems, such as GaAs/AlAs, presents significant challenges. Using MBE complex structures of thin layers may be grown with large concentrations and concentration gradients. Band mixing occurs at the interface between the GaAs and AlAs materials due to broken crystal symmetry. Accurate simulation of tunneling currents in quantum well structures must take into account tunneling through the quantum well, space charge effects, band mixing at the interface, and phonon scattering. There have been a number of examples in the literature of simulations that account for tunneling through the quantum well, and either space charge effects or band mixing at the interface but generally not both. Alternatively, Wigner based simulations may take into account scattering by Relaxation Time Approximation (RTA) [21]. For comparison to low temperature experiments phonon scattering may be ignored.

Tight binding simulations have been used in the past to determine tunneling currents but have not included space charge effects (i.e., the solutions were not self-consistent with Poisson's equation). However, tunneling currents may be significantly affected by space charge effects. For example, in some heterostructures significant hysteresis in the I/V curve results from the inclusion of space charge[43]. Until now self-consistent tight binding simulations have been primarily confined to determining band structures and offsets.

Chapter 4 .2 Tight Binding

The crystal Schrödinger equation is given by [44]

$$H\psi(r) = (H_{at} + \Delta U(r))\psi(r) = \xi(k)\psi(r), \qquad \text{(Chapter 4 .1)}$$

where H is the full Hamiltonian, H_{at} is the atomic Hamiltonian, and ΔU is the difference between the atomic potential and the periodic crystal potential. The solution at each atom is a linear combination of n atomic orbitals. The crystal wavefunction ψ is expanded in terms of Wannier functions ϕ by the equation

$$\psi(r) = \sum_R e^{ik\cdot R}\phi(r - R). \qquad \text{(Chapter 4 .2)}$$

The Wannier function is given by

$$\phi(r) = \sum_n b_n \psi_n(r), \qquad \text{(Chapter 4 .3)}$$

where ψ_n are orthogonal atomic orbitals. Multiplying by ψ_m^* and integrating gives

$$\left(\xi(k) - E_m\right)\int \psi_m^*(r)\psi(r)dr = \int \psi_m^*(r)\Delta U(r)\psi(r)dr, \qquad \text{(Chapter 4 .4)}$$

where E_m is the energy associated with ψ_m. These equations can be combined to form the equation

$$\left(\xi(k) - E_m\right)b_m = -\left(\xi(k) - E_m\right)\sum_n\left(\sum_{R\neq 0}\int \psi_m^*(r)\psi_n(r - R)e^{ik\cdot R}dr\right)b_n +$$

$$\sum_n\left(\int \psi_m^*(r)\Delta U(r)\psi_n(r)dr\right)b_n + \sum_n\left(\sum_{R\neq 0}\int \psi_m^*(r)\Delta U(r)\psi_n(r - R)e^{ik\cdot R}dr\right)b_n \qquad \text{(Chapter 4 .5)}$$

where the terms on the right hand side are small. Integrals with terms centered on different sites, or overlap integrals, are assumed to be small. The second term on the right hand side is small because the wave functions are small where ΔU is large. The left hand side is small because b_m is small except where ξ(k) is near E_m. It may be rewritten in the form

$$\xi(k) = E_m - \frac{\sum_n \left(\int \psi_m^*(r) \Delta U(r) \psi_n(r) dr \right) b_n + \sum_n \left(\sum_{R \neq 0} \int \psi_m^*(r) \Delta U(r) \psi_n(r - R) e^{ik \cdot R} dr \right) b_n}{b_m - \sum_n \left(\sum_{R \neq 0} \int \psi_m^*(r) \psi_n(r - R) e^{ik \cdot R} dr \right) b_n}$$

(Chapter 4 .6)

where the denominator may be assumed to be near one. This gives the final form

$$\xi(k) = E_m - \sum_n \left(\int \psi_m^*(r) \Delta U(r) \psi_n(r) dr \right) b_n + \sum_n \left(\sum_{R \neq 0} \int \psi_m^*(r) \Delta U(r) \psi_n(r - R) e^{ik \cdot R} dr \right) b_n$$

(Chapter 4 .7)

$$\xi(k) = E_m - \sum_n \left(\beta_{m,n} \right) b_n + \sum_n \left(\sum_{R \neq 0} \gamma_{m,n} e^{ik \cdot R} \right) b_n \,, \qquad ($$

Chapter 4 .8)

where $\beta_{m,n}$ and $\gamma_{m,n}$ are overlap integral values which may be determined by fits to empirical bands. A tight binding matrix based on these empirical values forms an energy eigenvalue problem whose solution is the band structure of the bulk material.

Solving for s like levels only requires one equation, p like levels require three, and d like levels require five equations. For sp^3 hybridization four equations are required. Sp^3 hybridization is present in sapphire and diamond

structures [45] but doesn't completely describe indirect conduction bands. In sp^3s^* hybridization five equations are required for each ion, there are six diagonal onsite energies, and seven transfer matrix elements.

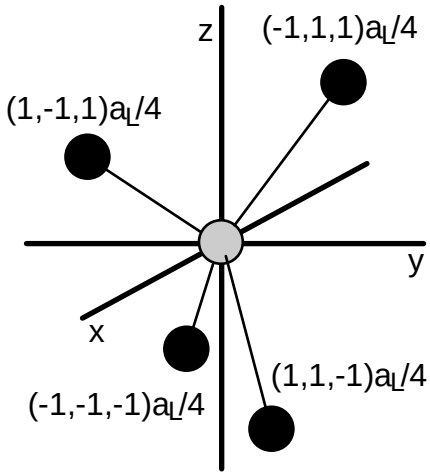

Figure Chapter 4 .1: This is the zinceblend nearest neighbor structure. The light sphere is an anion (a) and the dark spheres are cations (c).

Although the parameters published by Vogl[45] are generally useful, the effective mass values in some of the valleys conflict with published empirical values. This affects the resulting density of states for these materials. Parameters for the effective mass and minimas for GaAs and AlAs are shown in Table Chapter 4 .1 below.

The equations from Vogl's paper contain several mistakes. The correct equations for onsite energies are given by

$$E_{sc} - E_{sa} = \beta_s \cdot \left(\omega_{sc} - \omega_{sa}\right), \qquad \text{(Chapter 4 .9)}$$

$$E_{sc} + E_{sa} = E_{\Gamma 1c} - E_{\Gamma 1v}, \qquad \text{(Chapter 4 .10)}$$

$$E_{pc} - E_{pa} = \beta_p \cdot \left(\omega_{pc} - \omega_{pa}\right), \qquad \text{(Chapter 4 .11)}$$

$$E_{pc} + E_{pa} = E_{\Gamma 15c} - E_{\Gamma 15v}, \qquad \text{(Chapter 4 .12)}$$

$$E_{s^*a} - E_{s^*a} = \beta_{s^*} \cdot \left(\omega_{s^*c} - \omega_{s^*a}\right), \text{ and} \qquad \text{(Chapter 4 .13)}$$

$$E_{s^*c} + E_{s^*a} = E_{\Gamma 15c} - E_{\Gamma 15v}. \qquad \text{(Chapter 4 .14)}$$

The equations for overlap terms are constrained by eigen solutions at Γ and X symmetry points in terms of the already determined onsite energies. They are given by

$$V_{xx} = \frac{1}{2}\sqrt{\left(E_{\Gamma 15c} - E_{\Gamma 15v}\right)^2 - \left(E_{pc} - E_{pa}\right)^2}, \qquad \text{(Chapter 4 .15)}$$

$$V_{ss} = \frac{1}{2}\sqrt{\left(E_{\Gamma 1c} - E_{\Gamma 1v}\right)^2 - \left(E_{sc} - E_{sa}\right)^2}, \qquad \text{(Chapter 4 .16)}$$

$$V_{xy} = \frac{1}{2}\sqrt{\left[2 \cdot \left(E_{\Gamma 15c} - E_{X5v}\right)^2 - \sqrt{\left(E_{pc} - E_{pa}\right)^2 + 4 \cdot {V_{xx}}^2}\right]^2 - \left(E_{pc} - E_{pa}\right)^2}, \text{(Chapter 4 .17)}$$

$$V_{sa,pc} = \frac{\sqrt{\left(E_{sa} + E_{pc} - 2 \cdot E_{X1v}\right)^2 - \left(E_{sa} - E_{pc}\right)^2}}{2}, \qquad \text{(Chapter 4 .18)}$$

$$V_{pa,sc} = \frac{\sqrt{\left(Ec + E_{pa} - 2 \cdot E_{X3v}\right)^2 - \left(E_{sc} - E_{pq}\right)^2}}{2}, \qquad \text{(Chapter 4 .19)}$$

$$V_{s^*a,pc} = \frac{\sqrt{E_{s^*a} - E_{X1c}} \cdot \sqrt{E_{sa}E_{pc} - {V_{sa,pc}}^2 + \left(E_{X1c} - E_{pc} - E_{sa}\right) \cdot E_{X1c}}}{\sqrt{E_{sa} - E_{X1c}}}, \text{ and (Chapter 4 .20)}$$

$$V_{pa,s^*c} = \frac{\sqrt{-E_{s^*c} + E_{X3c}} \cdot \sqrt{-E_{pa}E_{sc} + V_{pa,sc}{}^2 - \left(E_{X3c} - E_{pa} - E_{sc}\right) \cdot E_{X3c}}}{\sqrt{E_{sc} - E_{X3c}}}.$$

(Chapter 4 .21)

These 13 matrix parameters are determined from empirical band structure energies $E_{\Gamma 1c}$, $E_{\Gamma 1v}$, $E_{\Gamma 15c}$, $E_{\Gamma 15v}$, E_{X1c}, E_{X3c}, and E_{X3v}, atomic orbital energies ω_{sa}, ω_{sc}, ω_{pa}, and ω_{pc}, and constants β_s, and β_p. Generally valence band information may be determined from bulk self-consistent calculations. If known, valence band offsets may be included by shifting the diagonal matrix elements of the appropriate materials.

Schrödinger's equation is given by the equation

$$\langle k, n | H | k', n' \rangle = E, \qquad \text{(Chapter 4 .22)}$$

where k and k' are wave numbers, n and n' are band indices, H is the tight binding Hamiltonian, and E is the eigen energy. The tight binding Hamiltonian has the form

$$H = \begin{bmatrix} H_a & V_{ac} \\ V_{ca} & H_c \end{bmatrix}, \qquad \text{(Chapter 4 .23)}$$

where H_a, and H_c are given by the equations

$$H_c = \begin{bmatrix} E_{sc} & 0 & 0 & 0 & 0 \\ 0 & E_{pc} & 0 & 0 & 0 \\ 0 & 0 & E_{pc} & 0 & 0 \\ 0 & 0 & 0 & E_{pc} & 0 \\ 0 & 0 & 0 & 0 & E_{s^*c} \end{bmatrix}, \text{ and} \qquad \text{(Chapter 4 .24)}$$

$$H_a = \begin{bmatrix} E_{sa} & 0 & 0 & 0 & 0 \\ 0 & E_{pa} & 0 & 0 & 0 \\ 0 & 0 & E_{pa} & 0 & 0 \\ 0 & 0 & 0 & E_{pa} & 0 \\ 0 & 0 & 0 & 0 & E_{s^*a} \end{bmatrix}, \qquad \text{(Chapter 4 .25)}$$

where E_{sa}, E_{sc} are the s orbital onsite energies, E_{pa}, E_{pc} are the p orbital onsite energies, and E_{s^*a}, E_{s^*c} are the s* orbital onsite energies calculated in equations (Chapter 4 .9)-(Chapter 4 .14). Off diagonal submatrices V_{ac} and V_{ca} are given by

$$V_{ac} = \begin{bmatrix} V_s^s \cdot g_0 & V_{pc}^{sa} \cdot g_1 & V_{pc}^{sa} \cdot g_2 & V_{pc}^{sa} \cdot g_3 & 0 \\ -V_{sc}^{pa} \cdot g_1 & V_x^x \cdot g_0 & V_y^x \cdot g_3 & V_y^x \cdot g_2 & -V_{s^*c}^{pa} \cdot g_1 \\ -V_{sc}^{pa} \cdot g_2 & V_y^x \cdot g_3 & V_x^x \cdot g_0 & V_y^x \cdot g_1 & -V_{s^*c}^{pa} \cdot g_2 \\ -V_{sc}^{pa} \cdot g_3 & V_y^x \cdot g_2 & V_y^x \cdot g_1 & V_x^x \cdot g_0 & -V_{s^*c}^{pa} \cdot g_3 \\ 0 & V_{pc}^{s^*a} \cdot g_1 & V_{pc}^{s^*a} \cdot g_2 & V_{pc}^{s^*a} \cdot g_3 & V_{s^*}^{s^*} \cdot g_0 \end{bmatrix}, \text{ (Chapter 4 .26)}$$

and

$$V_{ca} = V_{ac}^{\dagger}. \qquad \text{(Chapter 4 .27)}$$

The sapphire structure is described by

$$g_0(k_1,k_2,k_3) = \cos\left(\frac{k_1 \cdot a_L}{4}\right) \cdot \cos\left(\frac{k_2 \cdot a_L}{4}\right) \cdot \cos\left(\frac{k_3 \cdot a_L}{4}\right) - i \cdot \sin\left(\frac{k_1 \cdot a_L}{4}\right) \cdot \sin\left(\frac{k_2 \cdot a_L}{4}\right) \cdot \sin\left(\frac{k_3 \cdot a_L}{4}\right)$$

,(Chapter 4 .28)

$$g_1(k_1,k_2,k_3) = -\cos\left(\frac{k_1 \cdot a_L}{4}\right) \cdot \sin\left(\frac{k_2 \cdot a_L}{4}\right) \cdot \sin\left(\frac{k_3 \cdot a_L}{4}\right) + i \cdot \sin\left(\frac{k_1 \cdot a_L}{4}\right) \cdot \cos\left(\frac{k_2 \cdot a_L}{4}\right) \cdot \cos\left(\frac{k_3 \cdot a_L}{4}\right)$$

,(Chapter 4 .29)

$$g_2(k_1,k_2,k_3) = -\sin\left(\frac{k_1 \cdot a_L}{4}\right) \cdot \cos\left(\frac{k_2 \cdot a_L}{4}\right) \cdot \sin\left(\frac{k_3 \cdot a_L}{4}\right) + i \cdot \cos\left(\frac{k_1 \cdot a_L}{4}\right) \cdot \sin\left(\frac{k_2 \cdot a_L}{4}\right) \cdot \cos\left(\frac{k_3 \cdot a_L}{4}\right)$$

, and (Chapter 4 .30)

$$g_3(k_1,k_2,k_3) = -\sin\left(\frac{k_1 \cdot a_L}{4}\right)\cdot\sin\left(\frac{k_2 \cdot a_L}{4}\right)\cdot\cos\left(\frac{k_3 \cdot a_L}{4}\right) - i\cdot\cos\left(\frac{k_1 \cdot a_L}{4}\right)\cdot\cos\left(\frac{k_2 \cdot a_L}{4}\right)\cdot\sin\left(\frac{k_3 \cdot a_L}{4}\right).$$ (Chapter 4 .31)

If the matrix parameters are known the empirical band structure data that it represents may be determined from the same scheme that is used to determine the matrix elements in equations (Chapter 4 .9)-(Chapter 4 .14). First the valence band shift should be determined and removed from the matrix elements. Then the underlying band structure data is given by

$$\begin{bmatrix} E_{\Gamma 1c} \\ E_{\Gamma 1v} \end{bmatrix} = \frac{1}{2}\cdot\begin{bmatrix} 1 & 1 \\ 1 & -1 \end{bmatrix}\cdot\begin{bmatrix} E_{sc}+E_{sa} \\ \sqrt{4\cdot {V_{ss}}^2 + \left(E_{sa}-E_{sc}\right)^2} \end{bmatrix},$$ (Chapter 4 .32)

$$E_{\Gamma 15c} = \sqrt{4\cdot {V_{xx}}^2 + \left(E_{pa}-E_{pc}\right)^2},$$ (Chapter 4 .33)

$$E_{\Gamma 15v} = 0,$$ (Chapter 4 .34)

$$E_{X1v} = \frac{\left[\left(E_{sa}+E_{pc}\right) - \sqrt{4\cdot {V_{sa,pc}}^2 + \left(E_{sa}-E_{pc}\right)^2}\right]}{2},$$ (Chapter 4 .35)

$$E_{X3v} = \frac{\left[\left(E_{sc}+E_{pa}\right) - \sqrt{4\cdot {V_{pa,sc}}^2 + \left(E_{sc}-E_{pa}\right)^2}\right]}{2},$$ (Chapter 4 .36)

$$E_{X5v} = E_{\Gamma 15c} - \frac{1}{2}\sqrt{\left(E_{pc}-E_{pa}\right)^2 + 4\cdot V_{xx}} - \frac{1}{2}\sqrt{\left(E_{pc}-E_{pa}\right)^2 + 4\cdot V_{xy}},$$ (Chapter 4 .37)

$$\left(\left(E_{pc}-E_{X1c}\right)\cdot\left(E_{s^*a}-E_{X1c}\right) - {V_{s^*a,pc}}^2\right)\cdot\left(E_{sa}-E_{X1c}\right) = {V_{sa,pc}}^2\cdot\left(E_{s^*a}-E_{X1c}\right),$$ (Chapter 4 .38)

and

$$\left(\left(E_{pa}-E_{X3c}\right)\cdot\left(E_{s^*c}-E_{X3c}\right) - {V_{pa,s^*c}}^2\right)\cdot\left(E_{sc}-E_{X3c}\right) = {V_{pa,sc}}^2\cdot\left(E_{s^*a}-E_{X3c}\right),$$ (Chapter 4 .39)

where constant values are generally β_s=0.8, and β_p=0.6.

The parameters published by Vogl[45] do not result in agreement with published density of states (and therefore density of states effective mass) in main valleys. The T=77°K empirical parameters published by Boykin[46] provide better agreement as shown in Table Chapter 4 .1. These must be adjusted to the desired temperature to be used. The proposed technique for making this adjustment is in proportion to the energy gap function with temperature. Since the adjustment is small this should be sufficient. The energy gap for the direct Γ valley of GaAs[47] is given by

$$E_{g,\Gamma}(T) = 1.519 - \frac{5.408 \cdot 10^{-4} \cdot T^2}{(T + 204)}, \qquad \text{(Chapter 4 .40)}$$

and the ratio to the value at T=0°K is given by

$$R(T) = 1 - \frac{5.408 \cdot 10^{-4} \cdot T^2}{(T + 204) \cdot 1.519}. \qquad \text{(Chapter 4 .41)}$$

For the AlAs gamma valley

$$E_{g,\Gamma}(T) = 3.13 - \frac{1.833 \cdot 10^{-3} \cdot T^2}{(T + 1350)}, \text{ and} \qquad \text{(Chapter 4 .42)}$$

$$R_{\Gamma}(T) = 1 - \frac{1.833 \cdot 10^{-3} \cdot T^2}{(T + 1350) \cdot 3.13}. \qquad \text{(Chapter 4 .43)}$$

For the AlAs X valley

$$E_{g,\Gamma}(T) = 3.229 - \frac{1.137 \cdot 10^{-3} \cdot T^2}{(T + 1047)}, \text{ and} \qquad \text{(Chapter 4 .44)}$$

$$R_{X}(T) = 1 - \frac{1.137 \cdot 10^{-3} \cdot T^2}{(T + 1047) \cdot 2.229}. \qquad \text{(Chapter 4 .45)}$$

The difference between R_Γ and R_X is less than 0.22%. These may be used to scale all bands for any arbitrary temperature. Applying this to the empirical

band values $E_{\Gamma 1c}$, $E_{\Gamma 1v}$, $E_{\Gamma 15c}$, $E_{\Gamma 15v}$, E_{X1c}, E_{X3c}, E_{X3v}, ω_{sa}, ω_{sc}, ω_{pa}, and ω_{pc} new matrix parameters may be derived at room temperature[46].

	Vogl[45]	Boykin[46]	Vogl[45]	Boykin[46]
Material	GaAs		AlAs	
$E_{\Gamma 1c}$	1.55	1.538	3.04	3.136
E_{G1v}	-12.55	-12.582	-11.73	-11.754
E_{G15v}	0.0	0.0	0.0	0.0*
E_{G15c}	4.71	4.629	4.57	4.57
E_{X1v}	9.83	-9.83	-9.52	-9.945
E_{X3v}	-6.88	-6.88	5.69	-7.668
E_{X1c}	2.03	2.03	2.30	2.796
E_{X3c}	2.38	2.38	2.68	2.369
E_{X5v}	-2.89		-2.20	-1.789
m_{Γ}	0.119	0.0691	0.295	0.147
m_X	0.105	0.203	0.228	1.94
ΔE_v	0	0	0	0.6303
T (°K)	0	77	0?	77

Table Chapter 4 .1: These are band parameters from Vogl[45] and Boykin[46].

	77K	300K	77K	300K
Material	GaAs		AlAs	
E_{sa}	-8.39	-8.39000	-8.2663110	-7.93797
E_{pa}	1.07475	1.07475	0.3442887	0.42500
E_{s*a}	8.57475	8.57475	6.8442390	6.84424
E_{sc}	-2.65405	-2.65405	-1.6298230	-1.49230
E_{pc}	3.55475	3.55475	2.9476890	2.95360
E_{s*c}	6.70475	6.70475	6.0876890	6.08769
V_{ss}	-6.4513	-6.4513	-6.6642	-6.47258
V_{xx}	1.9546	1.9546	1.8780	1.82396
V_{xy}	4.77	4.77	3.86	3.74898
$V_{sa,pc}$	4.68	2.81494	5.6	5.43898
$V_{sc,pa}$	7.7	7.7	7.6	7.6
$V_{s*a,pc}$	4.85	4.06744	4.22	4.14617
$V_{pa,s*c}$	6.9	4.49966	8.3	8.14127
m_{Γ}	0.0691	0.633	0.147	0.152
m_X	0.203	0.035	1.94	0.049
ΔE_v	0	0	0.6303	0.53

Table Chapter 4 .2: The valence band offset at the GaAs/AlAs heterostructure interface at room temperature using the simple ratio.

The valence band offset at the GaAs/AlAs heterostructure interface is often assumed to be about 40% of the direct gap. At 0°K this is a valence band gap of 0.6392 eV. From Adachi[48] the valence band offset in eV is suggested to be given by

$$\Delta E_v = (0.51 \pm 0.04) \cdot x \qquad \text{(Chapter 4 .46)}$$

where x is the Al mole fraction ($Al_xGa_{(1-x)}As$). Also, theoretical calculations using self-consistent tight binding simulators show a valence band offset of 0.51 eV[49]. XPS measurements suggest 0.44 eV[49]. Other references suggest a value of 0.48 eV. There is significant research to suggest an offset somewhere in the 0.5 eV range[49-51]. The problem with choosing a 40% band gap resulting in a

valence band offset of about 0.64 eV is that it suggests that at the heterostructure interface the difference between E_Γ in GaAs and E_X in AlAs is very small, on the order of 0.067 eV. This value should be about 0.2 eV[52] which is consistent with a valence band offset of 0.51 eV. The validity of an estimate may be determined by simulating currents in GaAs/AlAs heterostructures. Some current simulations in the literature have been significantly higher than laboratory measurements[46,53]. Although internal carrier concentrations may not be well known reasonable bounds do suggest restrictions. Comparisons will be made between simulated and measured single barrier diode currents.

Chapter 4 .3 Band Structures

Good results in duplicating first conduction band and valence band of pseudopotential band structures have been shown in the literature[54]. Tight binding matrix parameters are determined by fitting to empirical band data [47].

In this simulation the tight binding parameters[46] were determined for room temperature and shifted to reflect a valence band offset of 0.54 eV. There remains significant controversy about the valence band offset. The resulting band structure is shown in Figure Chapter 4 .2.

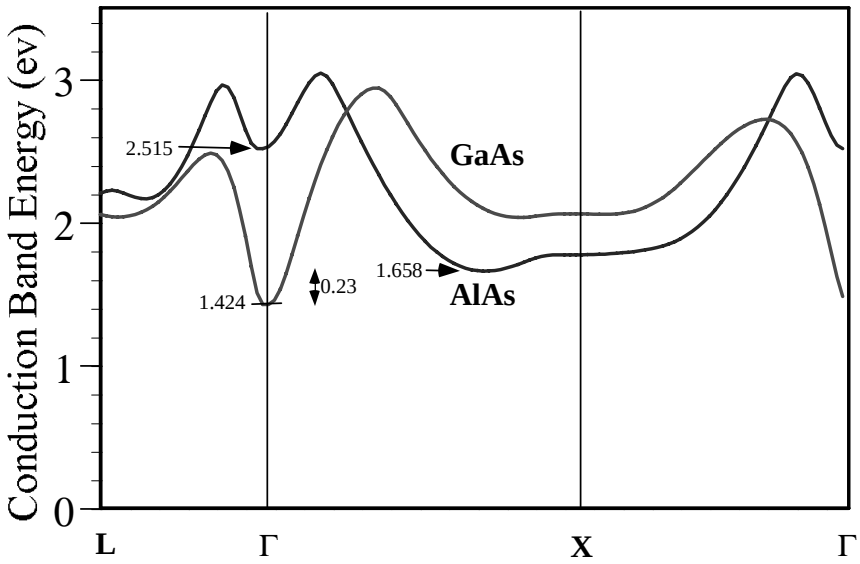

Figure Chapter 4 .2 This is the bandstructure of the first conduction band in GaAs and AlAs. A valence band offset of 0.54 eV is used.

These curves show the first conduction bands for GaAs and AlAs. A single barrier device may be formed by sandwiching an AlAs barrier by GaAs on either side. This forms a 1.09 eV barrier in Γ and 0.3 eV quantum well at X. The AlAs X valley is only about 0.23 eV above the GaAs Γ valley.

Chapter 4 .4 Discretization

The nearest neighbor sapphire structure is shown in Figure Chapter 4 .1. The spacing between anions and cations is $a_L/4$, where a_L is the lattice spacing. The one dimensional discretization is defined by the equation

$$V_{a,c} = V_{a,c}^{+} \cdot e^{ik_z a_L/4} + V_{a,c}^{-} \cdot e^{-ik_z a_L/4}, \qquad \text{(Chapter 4 .47)}$$

where the $V_{a,c}^{+}$, and $V_{a,c}^{-}$ are hopping matrices forward and backward one node, and k_z is the wavenumber in the z direction. The terms g_0 through g_3 defining the

sapphire structure in matrix , (Chapter 4 .26) are split among these two matrices and are given by

$$g_0^+ = \frac{1}{2}\left(\cos\left(k1\cdot {}^{a_L}\!/_4\right)\cdot\cos\left(k2\cdot {}^{a_L}\!/_4\right)+\sin\left(k1\cdot {}^{a_L}\!/_4\right)\cdot\sin\left(k2\cdot {}^{a_L}\!/_4\right)\right),\ ($$

Chapter 4 .48)

$$g_0^- = \frac{1}{2}\left(\cos\left(k1\cdot {}^{a_L}\!/_4\right)\cdot\cos\left(k2\cdot {}^{a_L}\!/_4\right)-\sin\left(k1\cdot {}^{a_L}\!/_4\right)\cdot\sin\left(k2\cdot {}^{a_L}\!/_4\right)\right),\ ($$

Chapter 4 .49)

$$g_1^+ = -\frac{i}{2}\left(\cos\left(k1\cdot {}^{a_L}\!/_4\right)\cdot\sin\left(k2\cdot {}^{a_L}\!/_4\right)-\sin\left(k1\cdot {}^{a_L}\!/_4\right)\cdot\cos\left(k2\cdot {}^{a_L}\!/_4\right)\right),(\text{Chap}$$

ter 4 .50)

$$g_1^- = \frac{i}{2}\left(\cos\left(k1\cdot {}^{a_L}\!/_4\right)\cdot\sin\left(k2\cdot {}^{a_L}\!/_4\right)+\sin\left(k1\cdot {}^{a_L}\!/_4\right)\cdot\cos\left(k2\cdot {}^{a_L}\!/_4\right)\right),\ ($$

Chapter 4 .51)

$$g_2^+ = \frac{i}{2}\left(\cos\left(k1\cdot {}^{a_L}\!/_4\right)\cdot\sin\left(k2\cdot {}^{a_L}\!/_4\right)-\sin\left(k1\cdot {}^{a_L}\!/_4\right)\cdot\cos\left(k2\cdot {}^{a_L}\!/_4\right)\right),($$

Chapter 4 .52)

$$g_2^- = \frac{i}{2}\left(\sin\left(k1\cdot {}^{a_L}\!/_4\right)\cdot\cos\left(k2\cdot {}^{a_L}\!/_4\right)+\cos\left(k1\cdot {}^{a_L}\!/_4\right)\cdot\sin\left(k2\cdot {}^{a_L}\!/_4\right)\right),($$

Chapter 4 .53)

$$g_3^+ = \frac{-1}{2}\left(\cos\left(k1\cdot {}^{a_L}\!/_4\right)\cdot\cos\left(k2\cdot {}^{a_L}\!/_4\right)+\sin\left(k1\cdot {}^{a_L}\!/_4\right)\cdot\sin\left(k2\cdot {}^{a_L}\!/_4\right)\right),(\text{Chap}$$

ter 4 .54)

and

$$g_3^- = \frac{1}{2}\left(\cos\left(k1\cdot {}^{a_L}\!/_4\right)\cdot\cos\left(k2\cdot {}^{a_L}\!/_4\right)-\sin\left(k1\cdot {}^{a_L}\!/_4\right)\cdot\sin\left(k2\cdot {}^{a_L}\!/_4\right)\right).($$

Chapter 4 .55)

There will be an overlap term between each combination of orbitals at these locations. In order to discretize the equations along z, arbitrarily, the overlap matrices are split into forward or υ = +, and backward or υ = - parts. These overlap matrices are given by

$$V^{\upsilon}{}_{\alpha.\alpha'} = \begin{bmatrix} V_s^s \cdot g_0^{\upsilon} & V_{p\alpha'}^{s\alpha} \cdot g_1^{\upsilon} & V_{p\alpha'}^{s\alpha} \cdot g_2^{\upsilon} & V_{p\alpha'}^{s\alpha} \cdot g_3^{\upsilon} & 0 \\ -V_{s\alpha'}^{p\alpha} \cdot g_1^{\upsilon} & V_x^x \cdot g_0^{\upsilon} & V_y^x \cdot g_3^{\upsilon} & V_y^x \cdot g_2^{\upsilon} & -V_{s^*\alpha'}^{p\alpha} \cdot g_1^{\upsilon} \\ -V_{s\alpha'}^{p\alpha} \cdot g_2^{\upsilon} & V_y^x \cdot g_3^{\upsilon} & V_x^x \cdot g_0^{\upsilon} & V_y^x \cdot g_1^{\upsilon} & -V_{s^*\alpha'}^{p\alpha} \cdot g_2^{\upsilon} \\ -V_{s\alpha'}^{p\alpha} \cdot g_3^{\upsilon} & V_y^x \cdot g_2^{\upsilon} & V_y^x \cdot g_1^{\upsilon} & V_x^x \cdot g_0^{\upsilon} & -V_{s^*\alpha'}^{p\alpha} \cdot g_3^{\upsilon} \\ 0 & V_{p\alpha'}^{s^*\alpha} \cdot g_1^{\upsilon} & V_{p\alpha'}^{s^*\alpha} \cdot g_2^{\upsilon} & V_{p\alpha'}^{s^*\alpha} \cdot g_1^{\upsilon} & V_{s^*}^{s^*} \cdot g_1^{\upsilon} \end{bmatrix}, \quad (\text{Chapter 4 .56})$$

where α and α' are a (anion) or c (cation), and $V_s{}^s$, $V_{pc}{}^{sa}$, $V_{sa}{}^{pc}$, $V_p{}^{s^*}$, $V_{s^*}{}^p$, $V_x{}^x$ and $V_y{}^x$ are also tabulated. $V_{a,c}{}^+ = V_{c,a}{}^-$ and $V_{c,a}{}^+ = V_{a,c}{}^-$ so that a Hamiltonian constructed of these components is Hermitian.

The energy eigenvalue problem may be written

$$H_E(k_X,k_y,k_Z)\,\Lambda = E\,\Lambda\,, \qquad \text{(Chapter 4 .57)}$$

where the Hamiltonian is given by

$$H_E = \begin{bmatrix} E^a & V_{a,c}^+ \cdot e^{ik_z a_L/4} + V_{a,c}^- \cdot e^{-ik_z a_L/4} \\ V_{c,a}^+ \cdot e^{ik_z a_L/4} + V_{c,a}^- \cdot e^{-ik_z a_L/4} & E^c \end{bmatrix}, \quad (\text{Chapter 4 .58})$$

which is k_1, k_2, and k_3 dependent, Λ is a matrix composed of the set of eigenvectors of (Chapter 4 .57), and E is a vector composed of its eigenvalues.

The energy bands of the bulk material may determined by the eigenvalues as a function of k_1, k_2, and k_3.

The nearest neighbor discretization is given by the Hermitian matrix

$$H = \begin{bmatrix} \ddots & \ddots & \ddots & \ddots & & & \\ V^{-}_{a,c_{i-1}} & E^{a}_{i} & V^{+}_{a,c_{i+1}} & & & & \\ & V^{-}_{c,a_i} & E^{c}_{i+1} & V^{+}_{c,a_{i+2}} & & & \\ & & V^{-}_{a,c_{i+1}} & E^{a}_{i+2} & V^{+}_{a,c_{i+3}} & & \\ & & & V^{-}_{c,a_{i+2}} & E^{c}_{i+3} & V^{+}_{c,a_{i+4}} & \\ & & & \ddots & \ddots & \ddots & \ddots \end{bmatrix}, \qquad (\text{Chapter 4.59})$$

where V_{ac}^{-} is the hopping matrix back one location and V_{ac}^{+} is the hopping matrix forward one location.

There are quasibound and unbound solutions. They are dealt with separately because ballistic transport is assumed to be elastic and so electrons from the contacts can not populate states below the contact energy levels. The quasibound state solutions are eigenvectors for eigenstates which are below the contacts.

There are two ways of solving for the wave equation for the unbound solution for a device at a range of nodes. One method is to use the transfer matrix method or Green's function recursion and the other is to build a single matrix and solve the matrix. The transfer matrix method is numerically unstable after a few hundred nodes. The transfer matrices may be used to build a matrix[46] or the underlying equations may be used to create the matrix.

Chapter 4 .5 Transfer Matrix method

In the case of heterostructures with interfaces [55] there is no translational symmetry. The boundary conditions are formulated in terms of solutions in three regions. The first and third regions are vacuum or bulk material with zero potential gradient. In the case of vacuum regions the solutions are in terms of simple plane waves. The second region contains the model with interfaces and potential changes. Solutions may be determined by reformulating the problem in companion form. Assuming nearest neighbors

$$H^m_{i,i-1}G^m_{i-1} + H^m_{i,i}G^m_i + H^m_{i,i+1}G^m_{i+1} = 0\,, \qquad \text{(Chapter 4 .60)}$$

where H are Hamiltonian matrix elements, i is the layer index, m is the number of orbitals, and G are the discretized Green's function solutions. The elements $H_{i,j}$ are m by m matrices and G are m by 1. Using this relation a companion form matrix may be formed[37] resulting in

$$\begin{bmatrix} -{H^m_{i,i-1}}^{-1}H^m_{i,i} & -{H^m_{i,i-1}}^{-1}H^m_{i,i} \\ 1 & 0 \end{bmatrix} \cdot \begin{bmatrix} G^m_i \\ G^m_{i+1} \end{bmatrix} = \begin{bmatrix} G^m_{i-1} \\ G^m_i \end{bmatrix} = e^{ik_\perp d} \cdot \begin{bmatrix} G^m_i \\ G^m_{i+1} \end{bmatrix},$$

(Chapter 4 .61)

where d is the distance between monolayers and $k_\perp$ is the wave vector in the crystal growth direction. The modal matrix oriented with the eigenvectors which decay to the right and then the eigenvectors which decay to the left may be used on each end to formulate these boundary relations.

The transfer matrix method is done by repeatedly applying equation (Chapter 4 .61), where T is given by

$$T^i\left(k_x,k_y,E\right)=\begin{bmatrix}-H^m_{i,i-1}{}^{-1}H^m_{i,i} & -H^m_{i,i-1}{}^{-1}H^m_{i,i}\\ 1 & 0\end{bmatrix}. \qquad \text{(Chapter 4 .62)}$$

For tight binding matrices this is the transfer from the anion to the cation, given by

$$T_{ac}\left(k_x,k_y,E\right)=\begin{bmatrix}-V_{ac}^{-1}E_a & -V_{ac}^{-1}V_{ac}^{+}\\ 1 & 0\end{bmatrix}\text{, and} \qquad \text{(Chapter 4 .63)}$$

the transfer matrix from the cation to the anion, given by

$$T_{ca}\left(k_x,k_y,E\right)=\begin{bmatrix}-V_{ca}^{-1}E_c & -V_{ca}^{-1}V_{ca}^{+}\\ 1 & 0\end{bmatrix}. \qquad \text{(Chapter 4 .64)}$$

The translation from one anion to the next is given by $T_{ac}\ T_{ca}$. This matrix is given by

$$T_{ac}T_{ca}=\begin{bmatrix}V_{ac}^{-1}E_aV_{ca}^{-1}E_c-V_{ca}^{-1}V_{ac}^{+} & V_{ac}^{-1}E_aV_{ca}^{-1}V_{ca}^{+}\\ -V_{ca}^{-1}E_c & -V_{ca}^{-1}V_{ca}^{+}\end{bmatrix}. \qquad \text{(Chapter 4 .65)}$$

These transfer matrices may be used to translate from the wave function at one end of the device to the other where $T^i = T_{ac}T_{ca}$ for node I is found using the equation

$$\begin{bmatrix}G_i^m\\ G_{i+1}^m\end{bmatrix}=T^i\left(k_x,k_y,E\right)^{-1}\cdot T^{i-1}\left(k_x,k_y,E\right)^{-1}\cdot T^{i-2}\left(k_x,k_y,E\right)^{-1}\ldots\begin{bmatrix}G_0^m\\ G_1^m\end{bmatrix}, \qquad \text{(Chapter 4 .66)}$$

where equation (Chapter 4 .61) forms a eigenvalue problem in $e^{ik_\perp d}$. The eigenvectors may be used to diagonalize the transfer matrix. In the first and third bulk regions where there is no potential change the eigenvalue problem from

equations (Chapter 4 .61) and . (Chapter 4 .65) may be used to transform from the plane wave basis to the orbital basis in the equations

$$\begin{bmatrix} G_0^m \\ G_1^m \end{bmatrix} = T^0 \cdot \begin{bmatrix} I \\ r \end{bmatrix}, \qquad \text{(Chapter 4 .67)}$$

$$\begin{bmatrix} I \\ r_b \end{bmatrix} = \left(T^0\right)^{-1} \cdot \begin{bmatrix} G_0^m \\ G_1^m \end{bmatrix}, \text{ and} \qquad \text{(Chapter 4 .68)}$$

$$\begin{bmatrix} \tau \\ r_f \end{bmatrix} = \left(T^n\right)^{-1} \cdot \begin{bmatrix} G_n^m \\ G_{n+1}^m \end{bmatrix}, \qquad \text{(Chapter 4 .69)}$$

where index i = 0 at the incident end and i = n at the transmitted end.

At index zero there is an incident plane wave with amplitude I, where the reflected wave r_b is unknown. At index n there is a transmitted wave with amplitude τ. The reflected wave on this end r_f is known and may be assumed to be zero.

Equations (Chapter 4 **.67)** - (Chapter 4 .69) may be used along with equation (Chapter 4 .66) to solve for the wavefunction in a device with a plane wave incident on one end and a transmitted plane wave on the other. To do this the eigenvectors must be arranged so that the associated eigenvalues are sorted with descending absolute values. For the ten band case there will be five eigenvalues whose absolute values are greater than or equal to one, and five with eigenvalues whose absolute values are less than or equal to one. At the incident end the eigenvalues greater than one are associated with plane waves traveling in a positive direction.

If there are m orbitals for the anion and m for the cation then the eigenvectors at each node will have 2m complex elements. By sorting the eigenvectors by the absolute value of their eigenvalue in descending order the traveling waves are always complex conjugates located at the m^{th} and $m+1^{th}$ element. For small $k_{||}$ and an energy above the conduction band minimum this may be assumed to be the Γ valley incident and reflected waves

$$\begin{bmatrix} t \\ r_f \end{bmatrix} = V^{-1} \cdot T^{i}\left(k_x, k_y, E\right)^{-1} \cdot T^{i-1}\left(k_x, k_y, E\right)^{-1} \cdot T^{i-2}\left(k_x, k_y, E\right)^{-1} \ldots V \cdot \begin{bmatrix} I \\ r_b \end{bmatrix}. \quad \text{(Chapter 4 .70)}$$

Here r_b and t are unknown and r_f and I are known.

Chapter 4 .6 Quantum Transmitting Boundary Method (QTBM)

Since the transform matrix method is unstable, the preferable solution method is to write the problem in terms of a matrix as in equation (Chapter 4 .59) plus additional equations from the boundary conditions. The boundary conditions are contained in (Chapter 4 .72), and (Chapter 4 .73).

$$\begin{bmatrix} I \\ r_b \end{bmatrix} = \begin{bmatrix} V^{-1}{}_{11} & V^{-1}{}_{12} \\ V^{-1}{}_{21} & V^{-1}{}_{22} \end{bmatrix} \cdot \begin{bmatrix} \varsigma_0^m \\ \varsigma_1^m \end{bmatrix} \quad \text{(Chapter 4 .71)}$$

$$I = V^{-1}{}_{11} \cdot \varsigma_0^m + V^{-1}{}_{12} \cdot \varsigma_1^m \quad \text{(Chapter 4 .72)}$$

$$r_f = V^{-1}{}_{1} \cdot \varsigma_n^m + V^{-1}{}_{22} \cdot \varsigma_{n+1}^m \quad \text{(Chapter 4 .73)}$$

The transmission coefficient may be calculated by the same method giving

$$\tau = V^{-1}{}_{1} \cdot \varsigma_n^m + V^{-1}{}_{22} \cdot \varsigma_{n+1}^m . \quad \text{(Chapter 4 .74)}$$

Chapter 4 .7 Self-Consistent Simulation

The Schrödinger Poisson iteration scheme was discussed in the previous chapter. Schrödinger Poisson self-consistent simulators iteratively determine the concentration and potential profiles. When the potential update is below a threshold, the current is determined from the final potential profile. Since the transmission spectrum is dependent upon this potential profile the current is highly dependent upon it as well. The concentration calculation will be discussed in section 4.8. If the initial potential profile guess is good, then few iterations may be necessary. No general statement may be made about the difference in convergence rates between tight binding and effective mass approximations. Figure 3.6 shows an example of the convergence of a simple case.

Chapter 4 .8 Concentration

Electron concentration may be associated with bound or traveling wave states. Concentration from bound states may be found by determining the energy eigenvalue and the eigenvector associated with it. Carrier concentration associated with traveling waves is found by summing the concentration over the energy band. For traveling wave states the matrix equation as shown in (Chapter 4 .59) is solved at a given k|| and energy with boundary condition equations (Chapter 4 .72) and (Chapter 4 .73). If the concentration for given bands is desired the density of states may be calculated for each band. The wavefunction solutions are in terms of Wannier orbitals. Density of states D for each band n may be determined by

$$D^n \propto \zeta^n * \zeta^n, \qquad \text{(Chapter 4 .75)}$$

$$\left\langle n \middle| \zeta^n \right\rangle = \sum_m \langle n|\Phi|m\rangle \left\langle m \middle| G^m \right\rangle, \qquad \text{(Chapter 4 .76)}$$

where Φ is the Hermitian transpose of the modal matrix Λ defined in equation (Chapter 4 .57). The wave vector k_z is determined using the transfer matrix based eigenvalue equation (Chapter 4 .61) specific to each node. The total density of states is generally sufficient if the only significant contribution to the carrier concentration, weighted by the Fermi Dirac distribution function, is from the desired band. The total density of states D is given by

$$D \propto \left\langle G^m \middle| G^m \right\rangle. \qquad \text{(Chapter 4 .77)}$$

The concentration is given from first principles by

$$C_i^n = \frac{2}{(2\pi)^3} \iint \int_{\xi=E(k\|)}^{E\max} \frac{\left|D_i^n\right|}{1+e^{(\xi-E_F)/kT}} \left(\frac{\partial k_z}{\partial \xi}\right) d\xi \, dk_x dk_y, \qquad \text{(Chapter 4 .78)}$$

where C_i^n is the electron concentration at node i in band n, E_F is the Fermi level, ξ is energy, k_x is the wavevector in the x direction, k_y is the wavevector in the y direction, k|| is the wavevector parallel to the surface, and Emax is the maximum energy in the band. Because of the symmetry of the problem ¼ of the Brillouin zone is integrated. The derivative $\frac{\partial k_z}{\partial E_z}$ may be determined numerically by determining the eigenvalue solution for the energy eigenvalue problem for a slightly incremented k_z, the wavevector perpendicular to the surface. If as an

approximation a k‖ is chosen rather than integrating over k_x and k_y the concentration calculation may be reduced to the form in Chapter 3.

Chapter 4 .9 Current

Current may be determined [46] by integrating over the Brillouin zone. The current density may be calculated using

$$J = \frac{2 \cdot e}{(2\pi)^3 \hbar} \int\int \int_{E_c \min(k\|)}^{E_c \max(k\|)} \left(f_{RIGHT}(E) - f_{LEFT}(E) \right) \cdot T\left(E, k||, V_{bias}\right) \cdot dE \; dk_x dk_y \text{ , (Chapter 4 .79)}$$

where $E_c$max and $E_c$min are the maximum and minimum conduction band energies possible within the band for k‖, $f_{RIGHT}(E)$ and $f_{LEFT}(E)$ are Fermi Dirac distributions for the right and left contact regions, and $T(E,k\|,V_{bias})$ is the transmission coefficient from (Chapter 4 **.74)**.

Since the triple integral in, (Chapter 4 .79) is obviously time consuming simplification to an integral of the form in (3.30) is desirable. The inclusion of a nonzero k‖ from equipartition may be done simply but it assumes the transmission coefficient depends only on E and V_{bias}, which is not generally true. Figure Chapter 4 .3 shows the transmission coefficient as a function of energy and k‖ as determined by (Chapter 4 **.74)**.

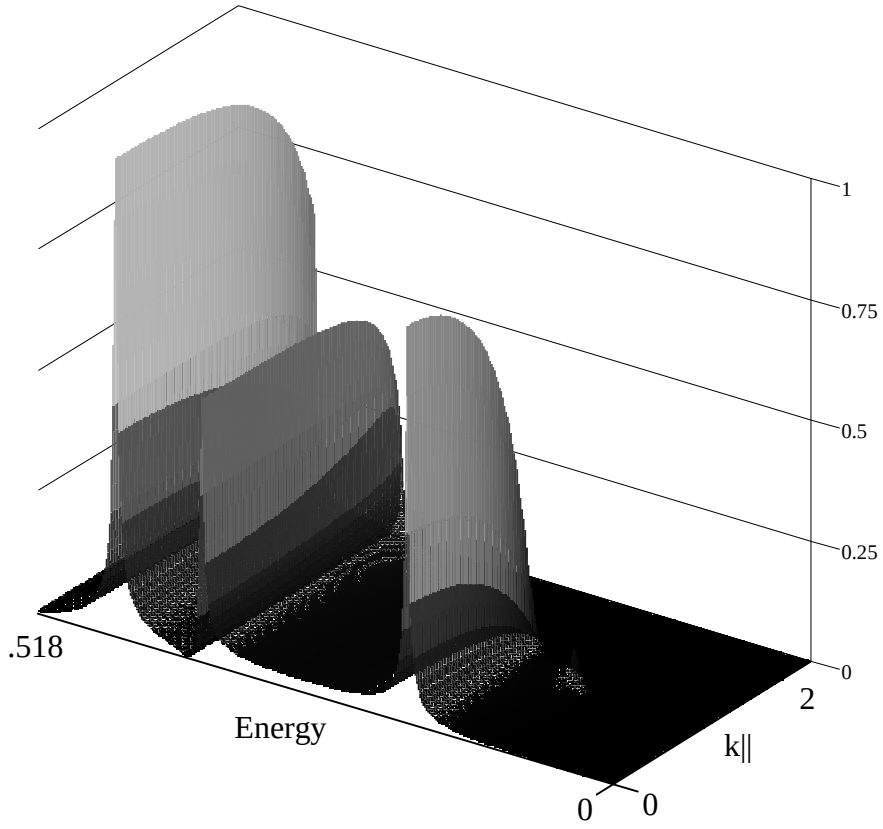

Figure Chapter 4 .3: This is a plot of the transmission coefficient versus k|| and energy. k|| is varied from 0 on the left to $2/a_L$ on the right where a is the node spacing. Energy is varied from 0 in front to about 20kT (0.518 eV) in the back. The transmission coefficient is highly dependent on k||.

Chapter 4 .10 Results

In this section the algorithm described in previous sections is tested using simple structures for which the answers are understood. These simple structures are used as building blocks for increasingly complex simulations. Since these quantum transport algorithms simulate only some of the models that describe the

physics controlling the behavior of devices, a comparison between simulations and laboratory measurements shows correspondence at best. As methods are developed that include more physical models the correspondence should improve. In any case the models described here do not include scattering and other processes. Interpretation of the simulation requires understanding the models used.

Because self-consistent tight binding calculations require correct concentration calculations, a test is done to show the compatibility of the tight binding and effective mass approximations. Concentration calculations in single material structures with modulation doping profiles should agree with Schrödinger Poisson self-consistent effective mass simulations. Several such comparisons have been done showing essentially identical results by these two methods. Agreement is shown between concentration and potential profiles at zero bias in Figure Chapter 4 .4 for a simple N+ / N- / N+ structure. Both are self-consistent simulations.

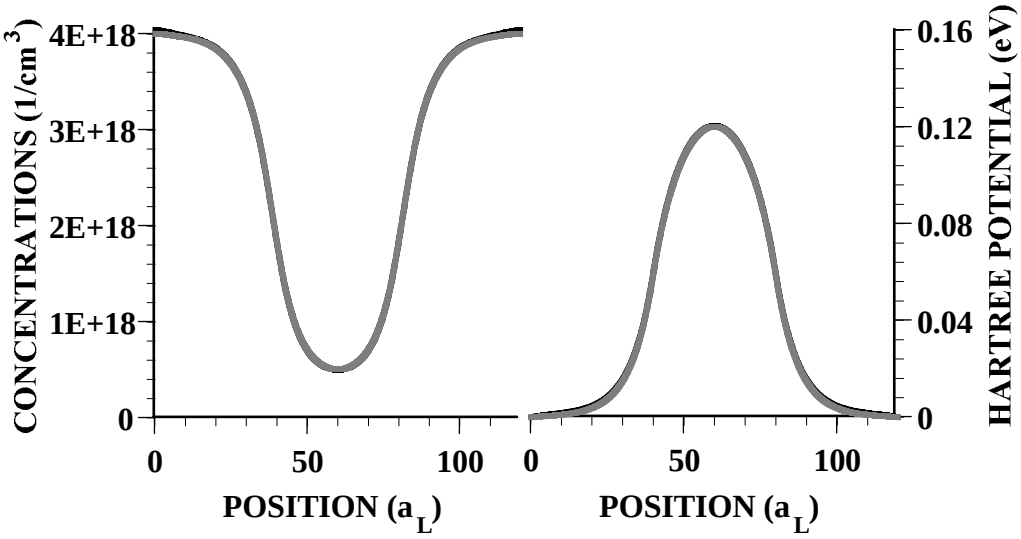

Figure Chapter 4 .4: This is a comparison between the self-consistent simulations using the tight binding and effective mass approximation. These are two curves, dark for tight binding and light for effective mass. These two curves are nearly identical making the separate curves difficult to distinguish. No adjustable parameters are used to achieve a match beyond reasonable band and effective mass parameters. Here the density of states (DOS) of the first conduction band is used. The calculation using the total DOS gives the same results.

Simulation of a device containing band mixing should not show agreement between tight binding and single valley effective mass approximations. A single barrier device is such a structure because band mixing occurs between the Γ and X valleys at the GaA/AlAs interface. In Figure Chapter 4 .5 a tight binding simulation shows a concentration of about $7x10^{16}$ (cm^{-3}) in the barrier. The effective mass simulation shows only evanescent waves in the barrier.

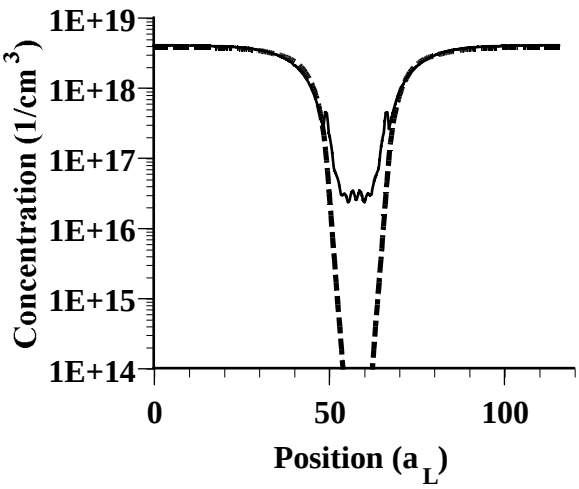

Figure Chapter 4 .5: This concentration profile shows a comparison between tight binding and effective mass approximation simulations of a 100 Å AlAs barrier. The solid line shows the tight binding concentration which is about $7x10^{16}$ cm^{-3} in the barrier. Since the effective mass waves are evanescent in the barrier, there is very little concentration in the dashed curve.

Self-consistent simulations of single barrier diodes with the tight binding and effective mass approximations should show significant differences. Simulations of the single barrier device structure shown in Figure Chapter 4 .6 were done at 77K. The resulting potential and concentration solutions are shown in Figure Chapter 4 .7. As expected there is significant concentration accumulation on the up wind side and depletion on the down wind side of the barrier. Current simulations of a 5 ML diode in Figure Chapter 4 .8 show Negative Differential Resistance (NDR) at about 0.3 and 0.4 volts and for a 7 ML diode show NDR particularly around 0.41 volts . NDR has been experimentally observed for a single barrier diode at low temperature [56]. Other tight binding current simulations of single barrier devices have shown current densities that are significantly too large [46]. This is because of the tight binding parameters chosen

and because the simulations were not self-consistent. The simulations shown here are in good agreement in general shape and magnitude with simpler simulations and laboratory measurements[57].

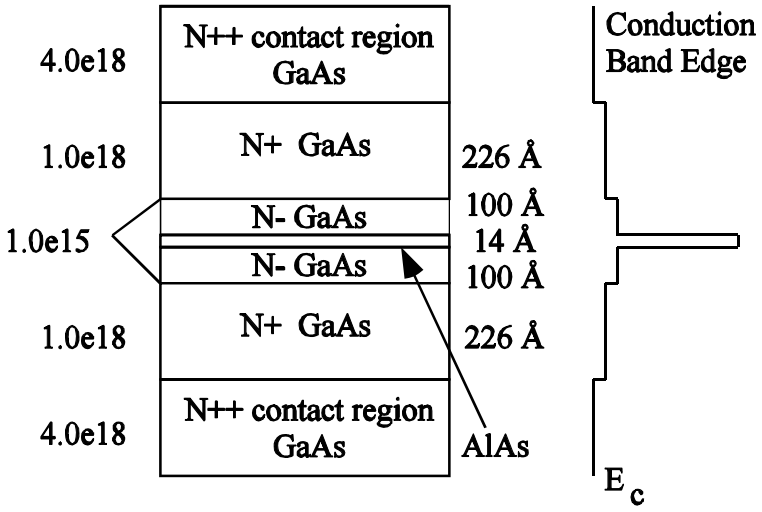

Figure Chapter 4 .6: This is a single barrier device structure in the GaAs/AlAs materials system. Here the AlAs barrier is 14 Å or about 5 ML.

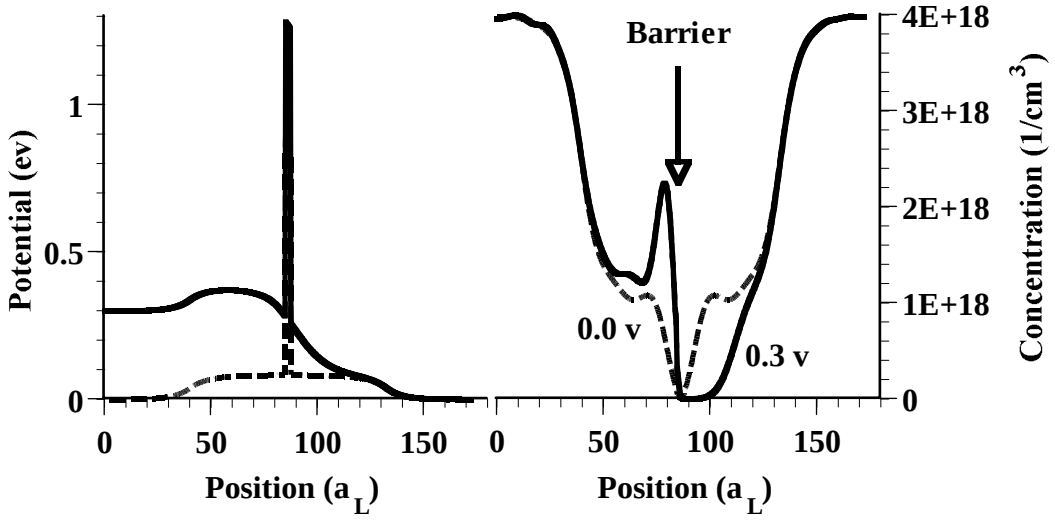

Figure Chapter 4 .7: Potential profiles are shown on the left at zero and 0.3 volts bias. Electron concentration is shown to the right for these two cases. In both cases the solid curve is for the 0.3 volt bias case. Note concentration increase on upwind side of the barrier at position 85.

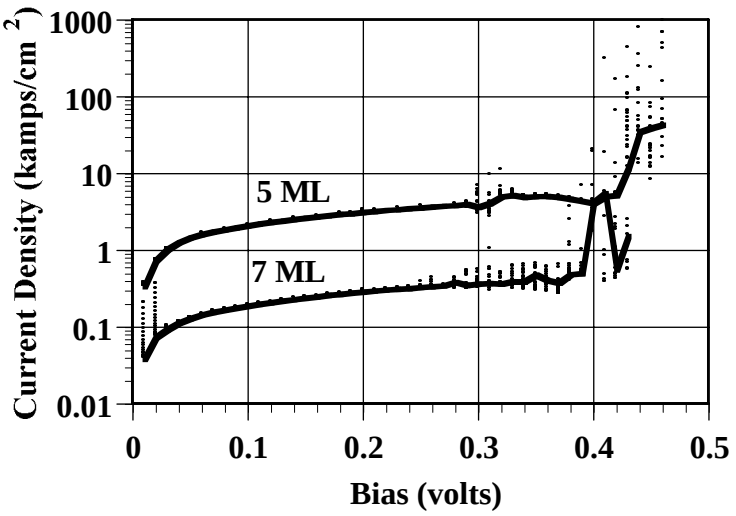

Figure Chapter 4 .8: Current density versus bias is shown for 5 ML and 7 ML AlAs barriers. The dots are intermediate points as convergence occurs. These simulations are done at 77K.

The next structure in increasing complexity to be considered is the DBRTD. For various applications it is desirable to calculate the peak and valley currents and voltages of these devices. Simulations based on the effective mass approximation generally show very low valley current which does not agree with laboratory measurements. This is primarily because this elastic model does not account for scattering of electrons into resonances, tunneling through the AlAs barrier by coupling between Γ-X-Γ valleys, and self-consistent effects due to not considering these effects in the concentration calculations. By modeling various of these effects comparison with laboratory measurements should indicate their relative importance.

The DBRTD structure simulated is shown in Figure Chapter 4 .9. The DOS function is shown at several points in the device structure in Figure Chapter 4 .10 as well as the transmission spectrum. Note that transmission is greater than

in the effective mass approximation because of the additional transmission path through Γ-X-Γ. Comparisons of self-consistent potentials and concentrations using tight binding show higher concentration in the region of the barrier as expected, and potential about 13% higher in the heterostructure region when compared to the effective mass approximations. This is significant because this large a band mixing effect on the potential effects the transmission spectrum and current, as shown in Figure Chapter 4 .11. The potential and concentration profiles at zero and 0.30 volts bias are shown in Figure Chapter 4 .12. Concentration accumulations are present in the conduction band notches created on the upwind side of the two barriers as expected.

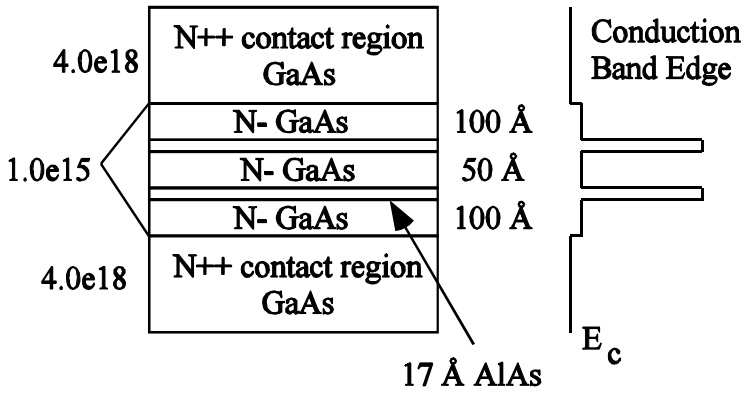

Figure Chapter 4 .9: This is the DBRTD device structure. It is a symmetric structure with a 50 Å heterostructure quantum well with 17Å AlAs barriers.

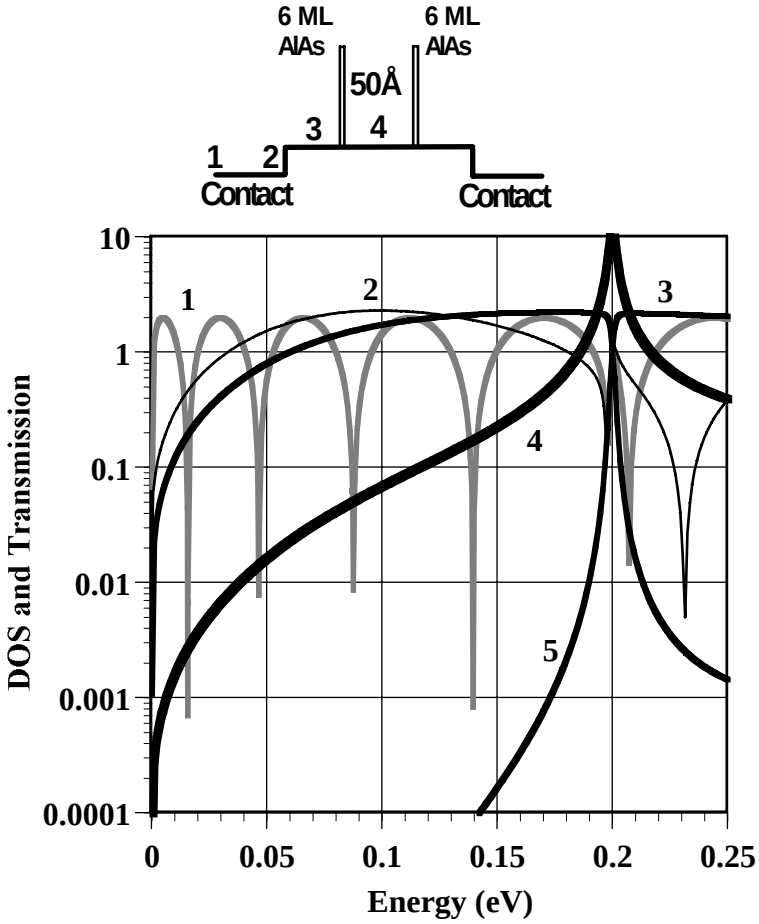

Figure Chapter 4 .10: This is the density of states (DOS) and transmission (τ) at several locations in the DBRTD device shown above the graph. Curve 1 corresponds to the beginning of the device at the contact, curve 2 corresponds to the end of the N++ region, curve 3 corresponds to the N- region adjacent to the barrier and curve 4 corresponds to the heterostructure quantum well. Note that the transmission coefficient in curve 5 peaks at about 0.18 eV. This coincides with the peak in the DOS spectrum of curve 4 which is the heterostructure quantum well. All other curves show a minimum at this energy indicating the electron lifetime is small except in the well. The other maxima and minima particularly in curve 1 are due to interference between incident wave and the wave reflected from the barrier. The transmission coefficient is larger than in Figure 3.5.

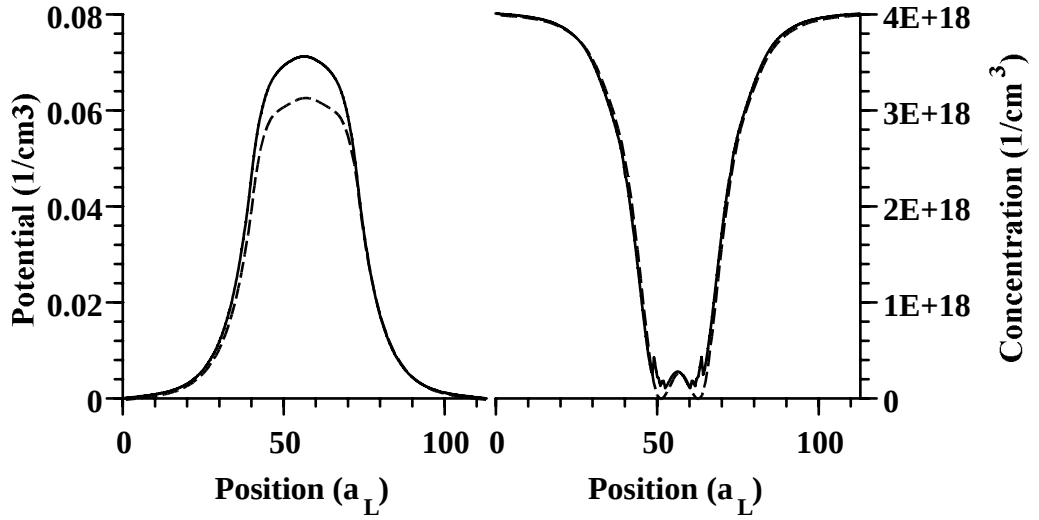

Figure Chapter 4 .11: This figure shows the potential and concentration profile for this DBRTD. The solid curve is the tight binding approximation and the dashed curve is the effective mass approximation. Note that the concentration is very similar except in the barrier region where the tight binding concentration is larger, as expected. As a consequence the potential profile from the tight binding simulation is about 13% larger.

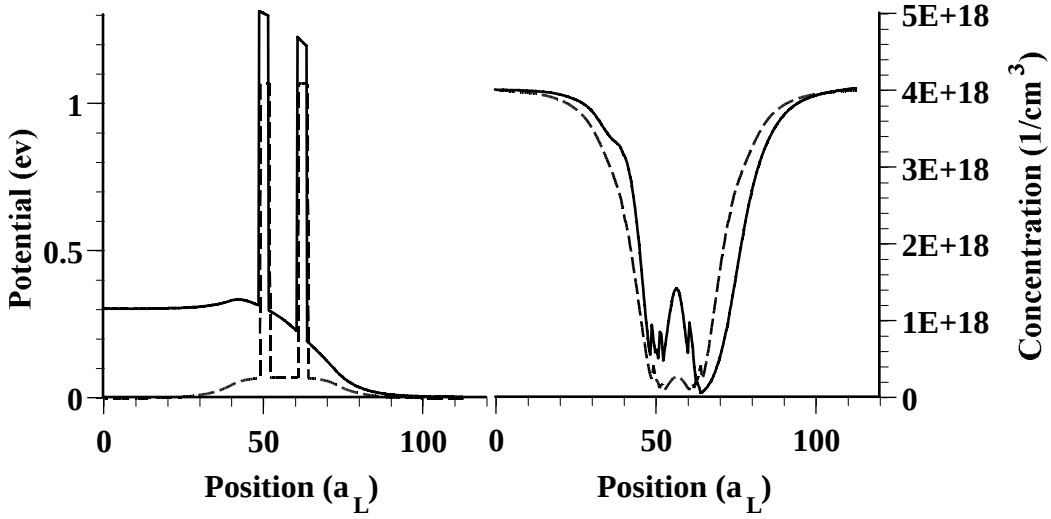

Figure Chapter 4 .12: These are the tight binding simulation potential and concentration profiles at zero and 0.30 volts bias. Note the upwind potential barrier at position 40.

A transmission spectrum for this device is shown in Figure Chapter 4 .13. It shows a transmission peak at 0.18 eV and a Fano resonance at about 0.36 eV. Fanno resonances are resonance-antiresonance pairs. The resonance is due to the well in the GaAs/AlAs/GaAs X valley and the antiresonance is due to cancellation of Γ-X by Γ-Γ evanescent waves in the barrier where they are π out of phase and the same magnitude [29].

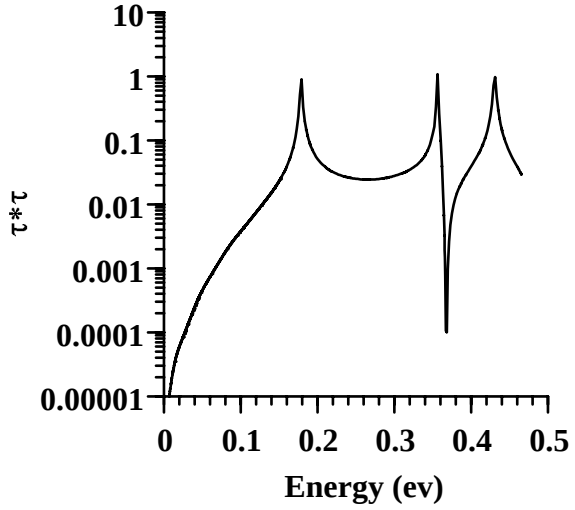

Figure Chapter 4 .13: This is the DBRTD transmission spectrum. The resonance at about 0.18 eV is shown as well as at 0.36 eV and 0.42 eV. The resonance at 0.36 eV is a resonance-antiresonance pair (a Fanno resonance) caused by interference between Γ-Γ and Γ-X waves. This is confirmation of Γ-X band mixing.

Γ-X-Γ coupling increases the transmission coefficient shown in Figure Chapter 4 .10 compared to that shown with the effective mass approximation in Figure 3.5. A comparison between currents from tight binding and effective mass approximation are shown in Figure Chapter 4 .14. The potential profile may be determined by several methods. A first order approximation may be made by

straight line segments. A better approximation may be made by adding a self-consistent zero bias solution to the straight line solution. The best and most time consuming approximation may be made using a full self-consistent simulation. Laboratory measurements show a peak current density of about 42 killoamps/cm^2 (kamps/cm^2) which agrees well with the effective mass and tight binding self-consistent simulations. The straight line potential approach has significantly higher current at the peak and lower peak voltage. This is because the upwind barrier shown in Figure Chapter 4 .12 is not modeled.

The peak voltage is at about 0.21 volts bias. Laboratory measurements shown in Figure 2.3 indicate a peak voltage at about 0.67 volts bias. The difference between peak and valley biases is about 0.25 volts. The self-consistent simulation shows a difference of about 0.2 volts. Non self-consistent simulations show a smaller potential difference. Since the peak to valley differences are similar this suggests a contact voltage drop of about 0.46 volts.

Laboratory measurements indicate a valley current of about 12 kamps/cm^2. The effective mass simulations show a valley current of less than 2 kamps/cm^2. Tight binding simulations show a valley current of about 10 kamp/cm^2. These simulations show more rounded current functions than observed in the laboratory. This is probably because of upwind barrier height which is sensitive to assumptions made about the GaAs background concentration. This suggests a higher background assumption than in the simulations. Values of 10^{15} and 10^{16} cm^{-3} have been tried.

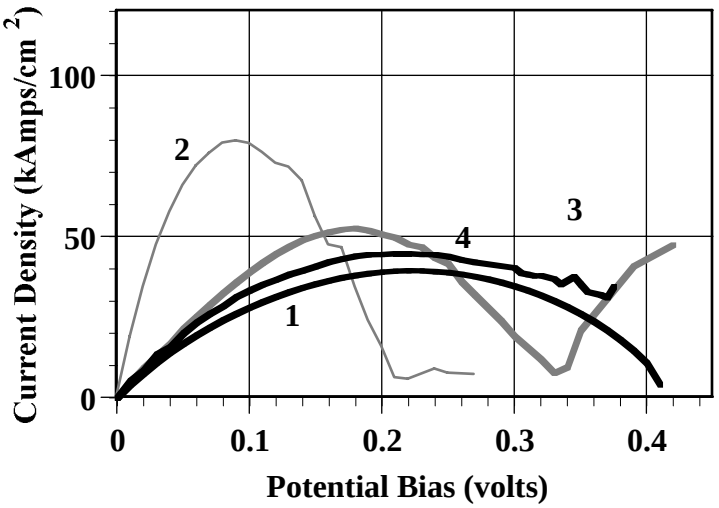

Figure Chapter 4 .14: This is a plot of current density versus bias voltage for this DBRTD using several assumptions. Curve 1 is a self-consistent simulation based on the effective mass approximation. Curve 2 is a non self-consistent tight binding simulation assuming a straight line potential approximation. Curve 3 is a non self-consistent tight binding simulation assuming a better potential approximation. Curve 4 is a self-consistent tight binding simulation.

MODFET's and the RTD's described earlier have significant similarities. Quantum transport models may allow simulation to optimally design complex MODFET structures. Here a simple structure[58] shown in Figure Chapter 4 .15 has been simulated as an example of the issues involved. Potential and concentration profiles from a zero bias tight binding simulation and a Thomas-Fermi simulation are shown in Figure Chapter 4 .16. In the tight binding simulation a notch is observed in the N++ pulse doped region of the AlGaAs layer. The oscillatory nature of the carrier concentration in this region may be due to quantum interference. In addition, because this is a transport model, due to the barriers formed by the potential profile on either side of this pulse doped region, the transmission of electrons from the contacts to this portion of the device is very

low. The source and drain contacts provide an additional path to supply electrons which should cause increased concentration in the pulse doped region and the channel. Concentration and potential profiles are shown in Figure Chapter 4 .16.

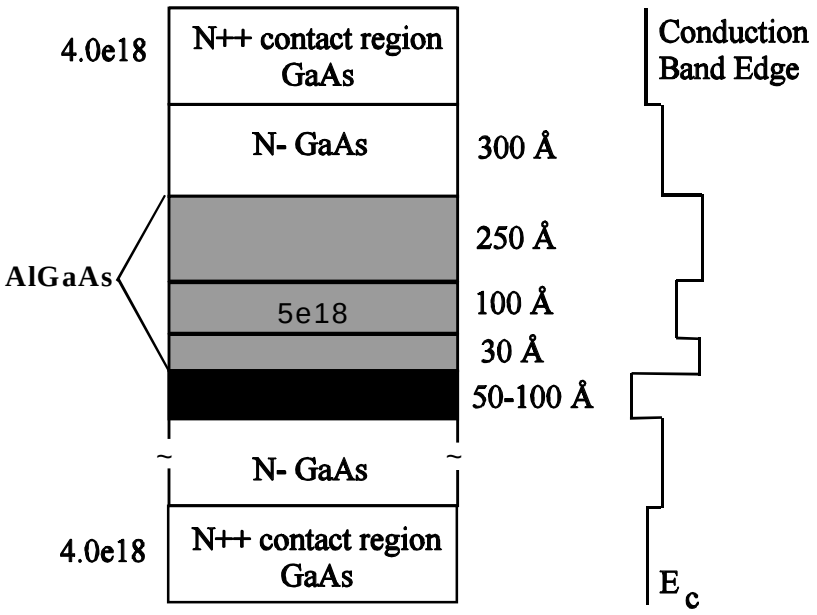

Figure Chapter 4 .15: This is a delta doped MODFET device structure.

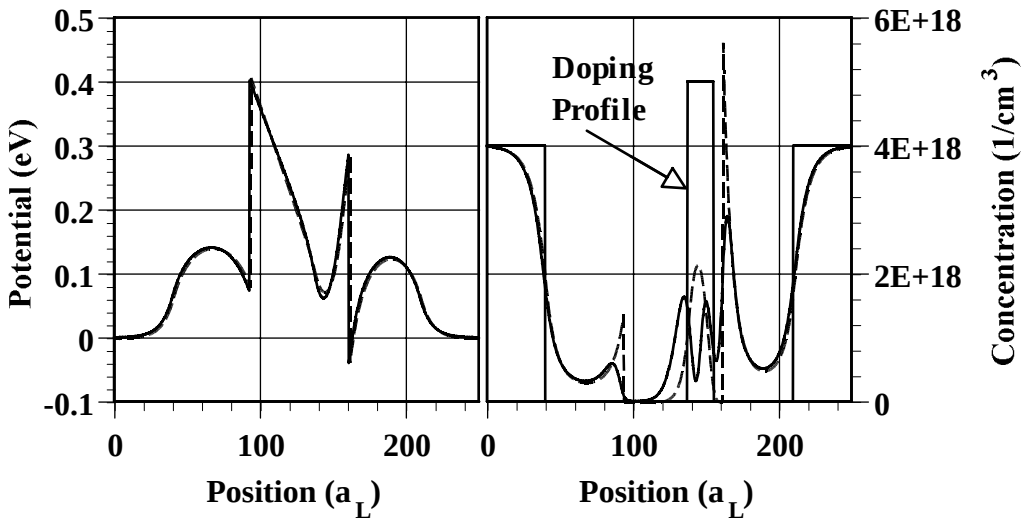

Figure Chapter 4 .16: The potential profile is shown to the left and the concentration profile is shown to the right. Two curves are shown. The dashed one is a Thomas Fermi simulation and the solid one is a tight binding simulation. Note the interference minimum that is located in the vicinity of the pulse doped region.

Chapter 4 .11 Summary

In this chapter space charge, interference, and tunneling effects have been included in simulations using tight binding formalism. The methods used have been explained and appropriate parameters chosen. These tight binding parameters represent accurate band structures. Greens function recursions may be used with adaptive solvers to get solutions or alternately single sparse matrices may be solved by LU decomposition. The latter method is employed here to obtain solutions using QTBM. Both concentration and current calculations are made and a practical method of determining the concentration in each band is formulated and tested. Concentration calculations are made integrating over k space and assuming k_T is determined by equipartition. Although the common

habit of assuming k_T to be determined in this way has been shown to be a poor approximation for current calculations it is computationally too expensive to do otherwise on the problems considered. Concentration and current calculations done using these methods give reasonable results for simple structures.

Low temperature current calculations of single barrier structures show small NDR features which have been observed empirically. This has been simulated incorrectly in the past by other authors [46]. In the simulations shown here small Γ - X conversion effects are observed for thin barriers. The concentration in the X valley in the AlAs layer effects the space charge solution. Resonances due to the X valley effect the transmission spectrum and so the current. Among other things this improves valley current calculations in RTDs.